# Characterizing the role of non-linear interactions in the transition to submesoscale dynamics at a dense filament

**Mara Freilich[1], Luc Lenain[1], Sarah T. Gille[1]**

[1]Scripps Institution of Oceanography, University of California San Diego

**Key Points:**

- Kinetic energy spectrum maintains a nearly continuous slope from 100 km to 1 km in an eastern boundary current region
- Between 1 and 10 km, non-linear interactions become dynamically important
- Cross-scale kinetic energy transfers are associated with shear strain in the observed front.

Corresponding author: Mara Freilich, `mfreilich@ucsd.edu`

**Abstract**

Ocean dynamics at the submesoscale play a key role in mediating upper-ocean energy dissipation and dispersion of tracers. Observations of ocean currents from synoptic mesoscale surveys at submesoscale resolution (250 m–100 km) from a novel airborne instrument (MASS DoppVis) reveal that the kinetic energy spectrum in the California Current System is nearly continuous from 100 km to sub-kilometer scales, with a $k^{-2}$ spectral slope. Although there is not a transition in the kinetic energy spectral slope, there is a transition in the dynamics to non-linear interactions at scales of $\mathcal{O}(1\ \text{km})$. Barotropic kinetic energy transfer across spatial scales is enabled by interactions between the rotational and divergent components of the flow field at the submesoscale. Kinetic energy flux is intermittent but can be large, particularly at submesoscale fronts. Kinetic energy is transferred both downscale and upscale from 1 km in the observations of a cold filament.

**Plain Language Summary**

Ocean dynamics at scales of 100 m–10 km, called the submesoscale, are important because they are associated with large velocity gradients and non-linear interactions. Large gradients lead to vertical velocity, which facilitates ocean-atmosphere interactions and ocean biological processes. Velocity gradients and non-linear processes combine to transfer kinetic energy from the large-scale flow to small-scale perturbations. This can lead to instabilities that dissipate energy in the ocean surface layer (rather than the seafloor). Here we analyze novel observations that provide insight into the distributions of velocity gradients and energy transfer at 1 km scale. Dynamics at these scales have previously been modeled, but have not been observed directly. We observe a transition where non-linear dynamics become more important at scales of order 10 km. We also introduce new interpretations of spectral analysis (analysis of energy and correlations across scales). Moreover, we analyze covariance of velocity gradient quantities and flow energetics to demonstrate that energy flux is episodic and localized at fronts. Together, these observations demonstrate that fronts play an important role in boundary-layer kinetic energy processes and highlight the evolution of upwelling filaments.

# 1 Introduction

Ocean processes in the surface boundary layer play a critical role in mediating the influence of atmospheric and climate processes on the ocean. Heating, wind-driven momentum input, and gas exchange occur at the sea surface and are transmitted through the boundary layer and into the ocean interior. The boundary layer also resides in the photic zone, where there is enough light for photosynthesis.

Submesoscale dynamics, the dynamics that operate at the spatial scales between the nearly geostrophically balanced mesoscale eddies (∼100 km scales in mid-latitudes) and three-dimensional turbulence (smaller than 100 m), are particularly important for these boundary layer processes (McWilliams, 2016). Submesoscales influence ocean biogeochemistry by modulating vertical transport (Mahadevan, 2016; Freilich et al., 2022) and influence air-sea interactions by modulating buoyancy and momentum transfer (Strobach et al., 2022). Submesoscale dynamics are hypothesized to facilitate a forward cascade of kinetic energy resulting in dissipation of eddy kinetic energy in the surface ocean (Capet et al., 2008b; Barkan et al., 2015; Srinivasan et al., 2023). However, submesoscale dynamics are also known to cascade energy upscale, strengthening mesoscale features (Schubert et al., 2020; Sandery & Sakov, 2017; Qiu et al., 2014). Determining the specifics of the dynamics in this transitional range of 100 m–100 km is essential for quantifying kinetic energy cycles in the ocean (Ferrari & Wunsch, 2009; McWilliams, 2016; Naveira Garabato et al., 2022).

The submesoscale is defined dynamically as the regime where the Rossby number, a non-dimensional parameter defined as $\text{Ro} = U/(fL)$, is order 1 with velocity $U$, hor-

izontal length scale $L$, and Coriolis parameter $f$. While geostrophic dynamics are thought to predominate at the mesoscale and larger, geostrophic balance can begin to break down at the submesoscale. At the larger end of the submesoscale, the surface quasigeostrophy framework presupposes that surface density fronts modify geostrophic balance (Klein & Lapeyre, 2009) while other theoretical results emphasize the role of non-linear advection in submesoscale dynamics (Barkan et al., 2019).

In this work we characterize the transition to submesoscale dynamics at scales smaller than 10 km and provide observational analysis of the kinetic energy cascade that has been hypothesized from models and theory. We observe submesoscale ocean surface velocity using remote sensing from airplanes during the submesoscale ocean dynamics experiment (S-MODE) field campaign (Farrar et al., 2020). We find substantial kinetic energy at the submesoscale, with a kinetic energy spectral slope that is nearly continuous from 100 to 1 km spatial scales. The dynamics that result in the spatial distribution of kinetic energy at the submesoscale are diagnosed through analysis of velocity cross spectra. These reveal that non-linear interactions between balanced and unbalanced dynamics contribute to submesoscale energy and illuminate the dynamics influencing upper-ocean velocity gradient distributions.

## 2 Methods

### 2.1 Remote sensing

The observations used in this study were collected by the DoppVis instrument (Lenain et al., 2023), a new sensor that is part of the Modular Aerial Sensing System (MASS Melville et al., 2016), that infers currents from optical observations the spatio-temporal evolution, i.e. dispersion relationship, of surface waves. Details about the DoppVis instrument are available in Lenain et al. (2023). The instrument package was installed on a Twin Otter DH-6 aircraft, flying at constant altitude above mean sea level (AMSL), with a flight profile consisting of repeated reciprocal straight tracks. Consistency between the reciprocal passes is used to validate velocity measurements. Velocity observations are binned to 256 m or 500 m prior to analysis.

Sea surface temperature observations are collected with a Flir SC6700SLS longwave IR camera (1 m resolution) and Heitronics KT19.85 II infrared thermometer (50 m resolution) (see Melville et al., 2016; Lenain et al., 2023, for details).

Observations from two field campaigns are considered in this study. The first field campaign sampled across a cold filament approximately 70 nautical miles offshore of California, as part of the NASA S-MODE program (Farrar et al., 2020). This region is subsequently referred to as the "filament region" and is the focus of this study. These observations occurred on November 3, 2021 from 18:23 to 23:33 UTC while flying at approximately 500 m AMSL and on November 5, 2021 from 22:40 to 23:00 UTC while flying at 940 m AMSL (Figure 1A,B). The observations from November 5 are binned at 256 m prior to analysis. The higher altitude enables collection of multiple data points in the cross-swath direction, resulting in a 1.5 km wide swath that is used to compute velocity gradients. The second field campaign collected observations across two counter-rotating eddies approximately 45 nautical miles offshore of San Diego on May 19, 2021 from 20:56 to 23:26 UTC (Lenain et al., 2023), as part of the "Platform Centric ASW Processing with Through-the-Sensor Data Assimilation and Fusion" project. This region is referred to as the "eddy region". Observations using a vessel mounted ADCP were collected under the long northwest-to-southeast leg of the DoppVis observations from May 19, 2021 10:00 to May 20, 2021 13:00 UTC.

### 2.2 Spectra

We analyze both the kinetic energy spectrum ($\hat{E}(f)$) and the cross spectrum ($\hat{S}(f)$) with 95% confidence intervals calculated following Bendat and Piersol (2011). Both the
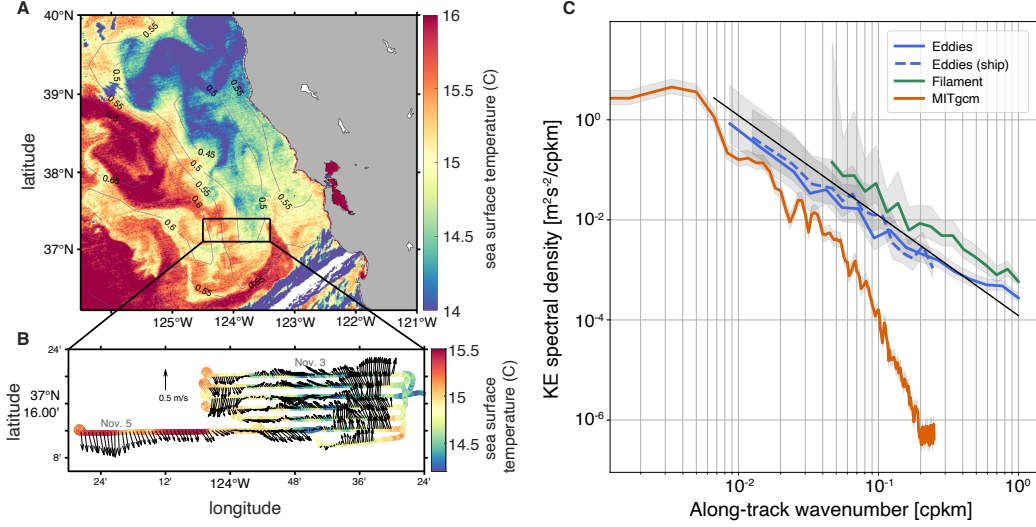
**Figure 1.** Velocity observations from both field campaigns situated in the large-scale context using satellite observations. (A) Satellite (MODIS Aqua) sea surface temperature in the filament region on November 3, 2021. Contours show sea surface height from AVISO. (B) DoppVis velocity across the sampled filament (black rectangle in panel A) is shown as vectors with sea surface temperature from the infrared thermometer. Two days of observations are shown, November 3 and November 5. The filament had shifted on November 5. (C) Kinetic energy spectral density as a function of along-track wavenumber from a 2 km resolution regional MITgcm model and two observational regions – the eddy region (May 2021) and the filament region (November 2021; panel B) – and two measurement platforms during May 2021 – DoppVis and a ship. The black line shows a $k^{-2}$ spectral slope.

kinetic energy spectra and the cross-spectrum between along-track and across-track velocity are computed using Welch's method with Hanning windows.

## 3 Results

### 3.1 Kinetic energy spectrum

The multi-scale nature of the flow is quantified using energy spectra, which can also be used to make inferences about the dominant dynamics governing the flow (Callies & Ferrari, 2013). The filament region is more energetic than the eddy region (Figure 1C), with approximately twice the amount of energy at nearly all spatial scales sampled. The kinetic energy spectra of the DoppVis observations have slopes that are approximately $k^{-2}$ (Figure 1C). The observed kinetic energy spectrum crossing the eddies has magnitude and spectral slope similar to that of the spectra from currents (15 m depth) taken with a vessel mounted acoustic Doppler current profiler (ADCP) on a nearby transect on the same day for 5–100 km scales.

This analysis extends the observations to smaller spatial scales than have been observed previously. Notably, these scales are smaller than those resolved by state-of-the-art global and regional models. As an example, we show the kinetic energy spectrum from a 2 km grid spacing MITgcm run (Mazloff et al., 2020) (Figure 1C, red line). The effective resolution of this model is 20 km with the velocity spectrum falling off steeply below that scale due to grid scale dissipation. Even at larger scales, both regions are more energetic than the 2 km grid spacing ocean model of the same region (the eddy region

is 5 times more energetic). The discrepancy between model and observations at lower wavenumbers is likely caused by an inverse cascade of submesoscale energy energizing surface mesoscale features in ways that are not represented in the model (Lévy et al., 2001; Mahadevan & Tandon, 2006) and by biased observational sampling toward more energetic features. It is important to note that only the larger end of submesoscale dynamics are resolved by 2 km models (Su et al., 2018; Sinha et al., 2022). This is especially important to keep in mind when considering cross-scale energy fluxes that may be modified by dynamics at small spatial scales.

The observed kinetic energy spectral slopes are consistent with previous observations from this region: a comprehensive analysis of surface velocities measured from vessel-mounted ADCPs in the California Current region from 1993–2004 found that the kinetic energy spectral slope in this region is approximately $k^{-2}$ or $k^{-5/3}$ at scales of 10 to 200 km (Chereskin et al., 2019). This is in contrast to the steeper spectral slope ($k^{-3}$) in more energetic regions such as the Antarctic Circumpolar Current, which implies geostrophic dynamics (Rocha et al., 2016). Modeling studies in the California Current System have found the kinetic energy spectrum to be continuous from the mesoscale to submesoscale, with a slope of approximately $k^{-2}$ (Capet et al., 2008a).

A range of dynamics could result in the observed spectral slope including internal gravity waves ($k^{-2}$), surface quasigeostrophy ($k^{-5/3}$), and fronts ($k^{-2}$) (Boyd, 1992; Lapeyre & Klein, 2006). The observations available in this study do not provide sufficient precision to distinguish these spectral slopes, nor can we identify whether the observed slope has transitions in the submesoscale regime.

### 3.2 Distributions of vorticity and divergence

One of the implications of a kinetic energy spectrum $E(k)$ with a $k^{-2}$ slope is that the velocity derivative spectrum $V(k)$ is flat because the spectra are linked through the relationship $V(k) = k^2 E(k)$. This means that as smaller spatial scales are observed, the variance of the distribution of velocity derivative quantities such as the vorticity and divergence will steadily increase.

The scale-dependent characteristics of velocity gradients are crucial for understanding submesoscale dynamics. The dynamical definition of submesoscale dynamics at Rossby number order 1 means that velocity gradients are of the same order of magnitude as the Coriolis frequency, such that the flow becomes more fully three dimensional (velocity divergence $\delta \sim U/L$), and the inertial term in the equations of motion ($u \cdot \nabla u \sim U^2/L$) is of the same order as the Coriolis term ($uf \sim Uf$).

The key velocity derivative quantities, divergence ($\delta = u_x + v_y$), vorticity ($\zeta = v_x - u_y$), and strain are related to each other through a system of coupled non-linear ordinary differential equations (c.f. Barkan et al., 2019). The strain is composed of shear strain ($\sigma_s = v_x + u_y$) and normal strain ($\sigma_n = u_x - v_y$).

In observations with 256 m resolution (submesoscale), which are only available for the filament case, we find that the vorticity is skewed positive (skewness 0.54, 90% confidence interval [0.49,0.69]), and the divergence is skewed negative (skewness -0.081, 90% confidence interval [-0.17, 0.043]) (Figure 2A,B), consistent with previous shipboard observations (Shcherbina et al., 2009; Rudnick, 2001). One explanation of this skewness is that the dynamical feedbacks are such that large negative relative vorticity is often unstable to symmetric and centrifugal instabilities but positive relative vorticity stabilizes the flow to these instabilities, and therefore a skewed distribution develops (Rudnick, 2001; Buckingham et al., 2016). Compared with anticyclonic fronts, cyclonic fronts also progress more slowly to singularities during frontogenesis, which could result in longer lived cyclonic fronts (Shakespeare, 2016). However, it is notable that strain-driven frontogenesis can suppress the growth of symmetric instability (Thomas, 2012). An alternate explanation is that the mechanism that generates the increased variance in relative vorticity generates a skewed distribution. One such mechanism would be strain-driven frontogenesis at the sea surface, which at an idealized front in the absence of dissipation
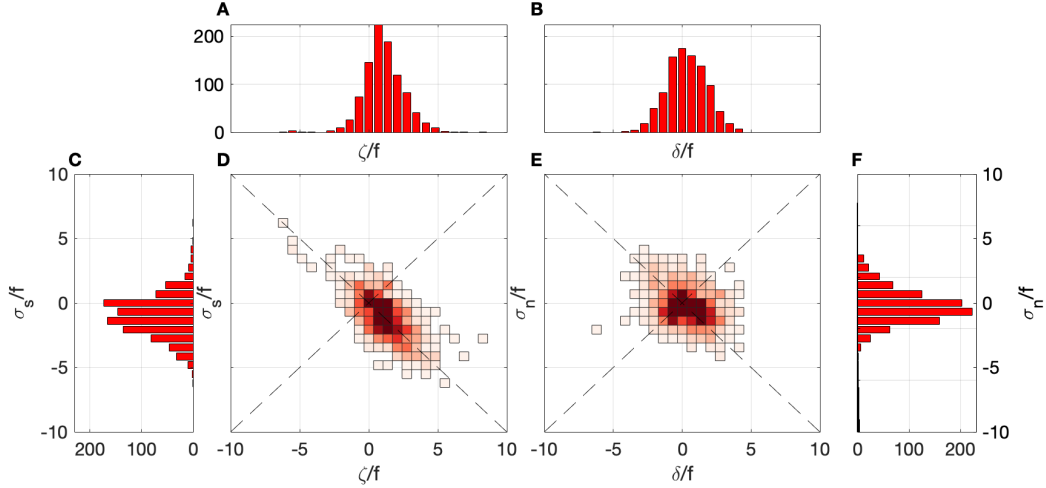
**Figure 2.** Velocity gradients in the filament observed on October 5 displayed as PDFs of (A) vorticity ($\zeta$), (B) divergence ($\delta$) (C) shear strain ($\sigma_s$), and (F) normal strain ($\sigma_n$), all normalized by $f$, along with joint PDFs of vorticity and shear strain (D) and divergence and normal strain (F).

results in an infinitely sharp front in finite time with ageostrophic flow that has skewed distributions of divergence and vorticity (Hoskins & Bretherton, 1972; Barkan et al., 2019). The mechanisms of surface frontogenesis and instability to negative potential vorticity are interrelated, as they both arise from conservation of potential vorticity.

In the filament observations studied here, vorticity is strongly correlated with shear strain (Figure 2D). This arises not because of direct forcing of vorticity by shear strain but instead because $\sigma_s \approx u_y \approx -\zeta$ over much of the sampled domain (but $\zeta \approx v_x$ at the front shown in Figure 4). Shear strain and vorticity are correlated due to the relative stability of cyclonic vorticity at straight fronts (Buckingham et al., 2021). This provides an explanation for the strain–vorticity relationship that has been observed in high-resolution simulations (Balwada et al., 2021). However, there is not a strong correlation between divergence and normal strain ($\sigma_n = u_x - v_y$), likely due to the importance of baroclinic processes in the presence of divergence and vertical motion (Figure 2E).

### 3.3 Non-linear interactions

#### 3.3.1 Interactions between rotational and divergent flow

The approximately $k^{-2}$ spectral slope in both the filament and eddy regions is informative but inconclusive about the about the dominant dynamics operating in these regions. The nearly uniform slope across the observed spatial scales leaves open questions about the scales at which a transition to submesoscale dynamics may occur.

One commonly used diagnostic of dynamics from observational data is the 'wave–vortex' decomposition introduced by Bühler et al. (2014) and further developed by Bühler et al. (2017), which derives the spectra of the rotational (streamfunction) and divergent (potential) velocity components. In studies using shipboard ADCP observations, this decomposition has been applied to demonstrate that while the larger mesoscale flow is mostly rotational, the divergent component of the flow becomes increasingly important at the small mesoscale ($\mathcal{O}(10$ km$)$) (Callies et al., 2015; Rocha et al., 2016; Chereskin et al., 2019).

One of the assumptions of this method is that the velocity streamfunction and velocity potential are uncorrelated. With this assumption, the cross spectrum of the $u$ and $v$ velocity components is a superposition of the spectra of the streamfunction and ve-

locity potential. In this case, since spectra are real, the cross spectrum is real (Bühler et al., 2017).

However, the assumption that the velocity streamfunction and potential are un-correlated does not hold at the submesoscale, i.e. Ro$\sim \mathcal{O}(1)$, because temporal changes in velocity gradient quantities (vorticity, divergence, and strain) are coupled in this regime (Barkan et al., 2019), resulting in a correlation between rotational and divergent veloc-ity components. We are therefore able to diagnose the spatial scale where a shift to sub-mesoscale dynamics occurs as the scale at which the cross spectrum between the along-track and across-track velocity ($\hat{S}_{uv}$) is complex, meaning that the rotational and diver-gent flow components interact. The phase ($\phi_{uv}$) is significantly different from zero when the cross-spectrum is complex.

Furthermore, if the magnitude of the cross spectrum of the $u$ and $v$ velocity com-ponents is large when compared with the wavenumber spectra of $u^2$ and $v^2$ (i.e. large coherence), then the flow is anisotropic ($\mathbb{E}(uv) = 0$ for isotropic flows). Cross-spectra have rarely been used for analysis of the spatial distributions of ocean velocities. We demon-strate here that they could be a valuable tool, particularly in the non-linear regime of submesoscale dynamics.

The coherence, which is the normalized cross spectrum between the along-track and across track velocity, has contrasting dependence on spatial scale in the two regions stud-ied here (Figure 3A). In the eddy region (blue lines in Figure 3), the coherence is large at the largest spatial scales sampled ($\sim$100 km) and decreases steadily to 10 km scales after which it flattens out, but remains significantly different from zero. In the filament region (green lines), the coherence is also large at the largest spatial scales sampled ($\sim$10 km), decreases at scales larger than 6 km, and then increases again toward the smallest spa-tial scales sampled ($\sim$1 km). Fronts and filaments are expected to be anisotropic at the scale of the feature, as is observed. Note, in all observations considered here, the coher-ence is large enough to be statistically significant, allowing for analysis of the cross-spectral phase.
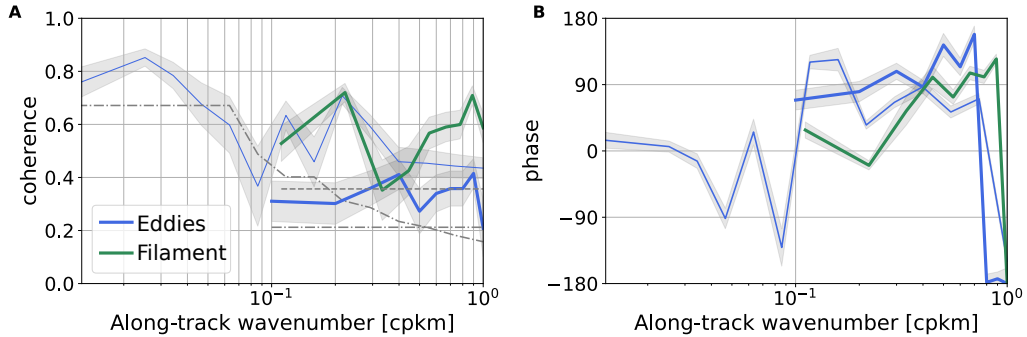


**Figure 3.** Flow anisotropy and non-linearity revealed by analysis of velocity cross spectrum. (A) Coherence as a function of wavenumber. The gray lines show the significance threshold (dashed and dot dash show filament and eddies, respectively) and the shading shows standard deviation. (B) Cross-spectrum phase. The thin lines in show the coherence computed from the long transects in the eddy region with 80 km windows while the dark lines show the coherence computed from every leg using 10 km windows.

The cross-spectral phase summarizes the relationship between the real and imag-inary parts of the cross spectrum. When the cross spectrum is purely real, the phase is 0° or 180°; when it is purely imaginary, the phase is ±90°. We find abrupt transitions at a scale slightly smaller than 10 km in the eddy region and 6 km in the filament re-gion, where the imaginary part of the cross spectrum becomes larger than the real part

(Figure 3B). This 6 km spatial scale is the same scale where the coherence increases in the filament region (suggesting increased anisotropy), providing consistent evidence of a change to increasingly non-linear frontal dynamics at these scales. By contrast, in a surface quasigeostrophic model, which neglects ageostrophic advection, the real part of the cross spectrum dominates at all spatial scales (Figure S1). During the eddy observations, the mixed-layer depth was measured at 40–55 m with some regions as shallow as 15 m. In contrast, for the filament observations, the mixed-layer depth was consistently approximately 35 m or shallower. As the mixed-layer stratification was approximately $3 \times 10^{-5}$, we expect a mixed-layer deformation radius of about 2–4 km for these locations, implying that the fastest growing baroclinic mode is around 8–24 km (Dong et al., 2020). The transition to non-linear ageostrophic dynamics observed here occurs in the approximate range of the scale of mixed-layer baroclinic instability.

There are a number of mechanisms that could be responsible for the interaction between rotational and divergent velocity. In the filament case, the interaction of the ageostrophic frontal divergence and larger scale geostrophic flow is likely the dominant mechanism. Here we find that the shift to a mostly imaginary cross spectrum is localized in the regions of largest velocity gradient in the filament situation (Figure S2). The eddy case likely encompasses a larger range of dynamics, including near-inertial oscillations modified by the vorticity of the observed features, frontal dynamics, and submesoscale vortices.

### 3.3.2 Spectral energy transfers

The distribution of kinetic energy across spatial scales reflects dynamics that are local in wavenumber, but importantly also reflects energy transfers across scales. At the submesoscale, major open questions remain regarding the direction of the energy cascade, the mechanisms that lead to a forward energy, and the rate of the forward energy cascade (McWilliams, 2016). Forward energy cascade precedes dissipation at small spatial scales, for example by surface boundary layer turbulence and secondary instabilities that may be associated with the energy cascade mechanism such as symmetric instability.

The energy transfer across scales can be quantified using coarse graining (Germano, 1992; Eyink, 2005; Aluie et al., 2018). The kinetic energy flux is defined here as

$$\Pi = -(\tau_{uv}(u_y + v_x) + \tau_{uu}u_x + \tau_{vv}v_y) \tag{1}$$

where $\tau_{ab} = \overline{ab} - \overline{a}\,\overline{b}$ and $\bar{\cdot}$ is a top hat filter. Positive values indicate a flux of energy toward smaller spatial scales, while negative values indicate a flux of energy toward larger spatial scales. The observations of the filament allow us to compute each of these terms directly. We use velocity observed on a 256 m grid and a top hat filter with a scale of 1 km to compute an instantaneous energy flux across the observed transect. Error is estimated using a bootstrapped 90% confidence interval and a velocity error of 0.1 m s$^{-1}$.

In the frontal regions in this flow, there is a strong forward energy flux localized in a 1 km region at the frontal outcrop (Figure 4A,B). The energy flux to smaller spatial scales is driven by the first term in equation 1 (Figure S3). This term involves the shear strain multiplied by the scale-dependent covariance between the along track and cross track velocity. In fact, over the entire 60 km section, there is a strong correlation between the shear strain and the kinetic energy flux (Figure 4C). This relationship may arise from certain aspects of the frontal relaxation case studied here and may not generalize to all fronts. For example, recent numerical results have suggested that divergence has a dominant role in submesoscale kinetic energy fluxes (Srinivasan et al., 2023). While our observations are not consistent with these modeling results, they also do not provide general evidence against the role of divergence in longer space and time averages.

The influence of the shear strain on the kinetic energy flux is modulated by the covariance between the $u$ and $v$ velocity components (or, equivalently, the anistropy of the flow), which becomes large below scales of 6 km in this filament region (Figure 3A). Barotropic
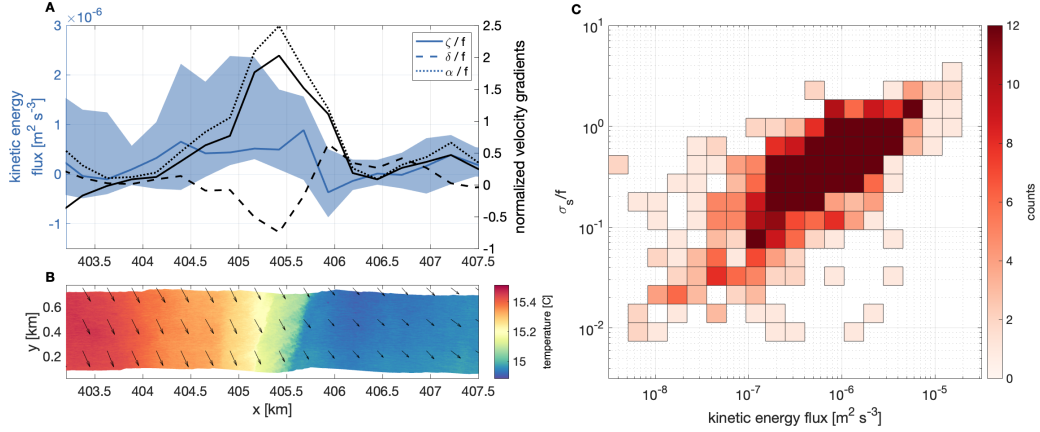
**Figure 4.** Spatial distribution of kinetic energy flux. (A) Kinetic energy flux across 1 km (shading shows the bootstrapped 90% confidence interval) and vorticity, divergence, and normalized strain ($\alpha = \sqrt{\sigma_n^2 + \sigma_s^2}$) at one of the fronts on the sampled transect. (B) Sea surface temperature measured from long wave infrared. Velocity is shown with vectors. (C) Joint probability density function of kinetic energy flux from the whole transect and shear strain.

shear instabilities extract kinetic energy from sheared mean flows when smaller scale features lean into the shear. This is the kinematic process at play in this forward energy cascade mechanism. However, the fronts that are analyzed here are restratifying, meaning that there is an upscale baroclinic energy transfer that co-occurs with the forward (barotropic) kinetic energy flux.

The observed kinetic energy flux is intermittent (Figure 4C), with the largest flux concentrated in small spatial scales even within the 60 km filament region observed here. Within the larger filament region (the 60 km sampling region), the kinetic energy flux varies over three orders of magnitude (Figure 4C). The typical kinetic energy flux across 1 km in the filament region is $\mathcal{O}(10^{-6} \text{ m}^2\text{s}^{-3})$. This rate is about an order of magnitude larger than the kinetic energy flux obtained from mooring based observations using a filter scale of 5 days (Naveira Garabato et al., 2022) and in a modeling study at 500 m spatial resolution (Srinivasan et al., 2023). Given that we present direct observations of the kinetic energy flux terms, this suggests that the magnitude of instantaneous kinetic energy flux has been underestimated by previous modeling and observational work.

## 4 Discussion and conclusion

The airborne observations presented here reveal a transition to non-linear submesoscale dynamics at scales of 6–10 km with implications for kinetic energy flux. The synoptic sampling from submesoscale to mesoscale allows us to extend an observational kinetic energy spectrum to scales below 1 km. Dense upwelling filaments such as the one observed here have an important role in the energetics of upwelling systems with submesoscale dynamics influencing the fate of upwelled waters.

We demonstrate that although there is not a clear change in the kinetic energy spectral slope, there is a transition in the dynamics to non-linear interactions that characterize submesoscales at scales of $\mathcal{O}(1 \text{ km})$. In particular, this transition is characterized by the interaction between divergent and rotational velocity components.

The observed transition to non-linearity has important implications for observations of ocean velocity from remote sensing. For example, the SWOT mission aims to infer mesoscale to submesoscale velocities through observation of sea surface height. These velocities are computed through geostrophic balance, which only accounts for the rota-

tional component of the flow. Not only do we find that a significant amount of the kinetic energy is likely in the divergent component of the flow at scales below 10 km in this region — and potentially at larger scales in more energetic regions (Callies et al., 2015) — but also that the rotational and divergent flows interact such that filtering of the divergent processes (e.g. waves) will not result in recovering the rotational component of the flow.

These observations are also the first direct observations of a *snapshot* of kinetic energy flux in the ocean. This allows us to investigate the relationships between the kinetic energy flux and hydrographic features. We find that kinetic energy flux is spatially intermittent but can be large ($10^{-6}$ m$^2$s$^{-3}$) at submesoscale fronts. The intermittency of kinetic energy flux has important implications for resolving the dynamics that contribute to an energy cascade. Due to the difficulty resolving scales ranging from mesoscale straining to turbulent dissipation in models, these observations — where that challenge is observationally addressed using a novel remote sensing platform — are particularly valuable. In the observations, kinetic energy is transferred both downscale and upscale from 1 km.

Recent modeling work has suggested that resolving frontogenesis is essential to accurate representation of submesoscale kinetic energy transfers (Naveira Garabato et al., 2022; Srinivasan et al., 2023). The observations analyzed here demonstrate a large forward energy transfer localized at fronts, although not exclusively during active large-scale frontogenesis. Recent work in the Gulf of Mexico, another region with active submesoscale, has hinted that a forward cascade of kinetic energy occurs at scales of 500 m–5 km (Balwada et al., 2022) in observations (with smaller scales during the summer) and at scales of 5 km in models (Srinivasan et al., 2023). Submesoscale dynamics in the Gulf of Mexico are driven by freshwater from river outflow, in contrast to the mesoscale features that are generated by coastal upwelling, which are the focus of this study. Srinivasan et al. (2023) analyzed kinetic energy fluxes in 500 m and 2 km resolution ocean models, which resolve dynamics at larger scales than those that are the focus of our study. They find an equipartition between strain-driven and convergence-driven forward energy cascade at submesoscale scales (Srinivasan et al., 2023). While we observe that the forward energy transfer is strain-driven in our observations, it is important to note that we have only one snapshot of a filament that appears to be partially restratifying, so this does not invalidate the role of convergence in forward energy flux.

These results suggest an out-sized role for fronts and filaments as hotspots of surface kinetic energy flux. Barotropic energy transfer is enabled by interactions between the rotational and divergent components of the flow field at submesoscale fronts. Fronts are spatially inhomogeneously distributed in the ocean and vary seasonally (Drushka et al., 2019; Mauzole et al., 2020), but the distributions of fronts are distinct from the distributions of mesoscale kinetic energy (Busecke & Abernathey, 2019). Surface kinetic energy dissipation may similarly vary substantially in space and time, but understanding how it varies relies on increased mechanistic understanding of the energetics of submesoscale features. Disentangling these would require more observations to establish the effect of particular submesoscale features on the regional statistics.

## Open research

All presented data are available at UCSD Library Digital Collection, https://doi.org/10.6075/J0F76CRK.

## References

Aluie, H., Hecht, M., & Vallis, G. K. (2018, February). Mapping the Energy Cascade in the North Atlantic Ocean: The Coarse-Graining Approach. *Journal of Physical Oceanography*, *48*(2), 225–244. doi: 10.1175/JPO-D-17-0100.1

Balwada, D., Xiao, Q., Smith, S., Abernathey, R., & Gray, A. R. (2021, September). Vertical Fluxes Conditioned on Vorticity and Strain Reveal Submesoscale Ventilation. *Journal of Physical Oceanography*, *51*(9), 2883–2901. doi: 10.1175/JPO-D-21-0016.1

Balwada, D., Xie, J.-H., Marino, R., & Feraco, F. (2022, October). Direct observational evidence of an oceanic dual kinetic energy cascade and its seasonality. *Science Advances*, *8*(41), eabq2566. doi: 10.1126/sciadv.abq2566

Barkan, R., Molemaker, M. J., Srinivasan, K., McWilliams, J. C., & D'Asaro, E. A. (2019). The role of horizontal divergence in submesoscale frontogenesis. *Journal of Physical Oceanography*, *49*(6), 1593–1618.

Barkan, R., Winters, K. B., & Smith, S. G. L. (2015, January). Energy Cascades and Loss of Balance in a Reentrant Channel Forced by Wind Stress and Buoyancy Fluxes. *Journal of Physical Oceanography*, *45*(1), 272–293. doi: 10.1175/JPO-D-14-0068.1

Bendat, J. S., & Piersol, A. G. (2011). *Random Data: Analysis and Measurement Procedures*. John Wiley & Sons.

Boyd, J. P. (1992, January). The Energy Spectrum of Fronts: Time Evolution of Shocks in Burgers Equation. *Journal of the Atmospheric Sciences*, *49*(2), 128–139. doi: 10.1175/1520-0469(1992)049⟨0128:TESOFT⟩2.0.CO;2

Buckingham, C. E., Gula, J., & Carton, X. (2021). The role of curvature in modifying frontal instabilities. Part I: Review of theory and presentation of a nondimensional instability criterion. *Journal of Physical Oceanography*, *51*(2), 299–315.

Buckingham, C. E., Naveira Garabato, A. C., Thompson, A. F., Brannigan, L., Lazar, A., Marshall, D. P., . . . Belcher, S. E. (2016). Seasonality of submesoscale flows in the ocean surface boundary layer. *Geophysical Research Letters*, *43*(5), 2118–2126. doi: 10.1002/2016GL068009

Busecke, J. J. M., & Abernathey, R. P. (2019, January). Ocean mesoscale mixing linked to climate variability. *Science Advances*, *5*(1), eaav5014. doi: 10.1126/sciadv.aav5014

Bühler, O., Callies, J., & Ferrari, R. (2014, October). Wave–vortex decomposition of one-dimensional ship-track data. *Journal of Fluid Mechanics*, *756*, 1007–1026. doi: 10.1017/jfm.2014.488

Bühler, O., Kuang, M., & Tabak, E. G. (2017, March). Anisotropic Helmholtz and wave–vortex decomposition of one-dimensional spectra. *Journal of Fluid Mechanics*, *815*, 361–387. doi: 10.1017/jfm.2017.57

Callies, J., & Ferrari, R. (2013). Interpreting energy and tracer spectra of upper-ocean turbulence in the submesoscale range (1–200 km). *Journal of Physical Oceanography*, *43*(11), 2456–2474.

Callies, J., Ferrari, R., Klymak, J. M., & Gula, J. (2015). Seasonality in submesoscale turbulence. *Nature communications*, *6*(1), 1–8.

Capet, X., McWilliams, J. C., Molemaker, M. J., & Shchepetkin, A. (2008a). Mesoscale to submesoscale transition in the California Current System. Part I: Flow structure, eddy flux, and observational tests. *Journal of Physical Oceanography*, *38*(1), 29–43.

Capet, X., McWilliams, J. C., Molemaker, M. J., & Shchepetkin, A. F. (2008b,

October). Mesoscale to Submesoscale Transition in the California Current System. Part III: Energy Balance and Flux. *Journal of Physical Oceanography*, *38*(10), 2256–2269. doi: 10.1175/2008JPO3810.1

Chereskin, T. K., Rocha, C. B., Gille, S. T., Menemenlis, D., & Passaro, M. (2019). Characterizing the Transition From Balanced to Unbalanced Motions in the Southern California Current. *Journal of Geophysical Research: Oceans*, *124*(3), 2088–2109. doi: 10.1029/2018JC014583

Dong, J., Fox-Kemper, B., Zhang, H., & Dong, C. (2020, September). The Scale of Submesoscale Baroclinic Instability Globally. *Journal of Physical Oceanography*, *50*(9), 2649–2667. doi: 10.1175/JPO-D-20-0043.1

Drushka, K., Asher, W. E., Sprintall, J., Gille, S. T., & Hoang, C. (2019, July). Global Patterns of Submesoscale Surface Salinity Variability. *Journal of Physical Oceanography*, *49*(7), 1669–1685. doi: 10.1175/JPO-D-19-0018.1

Eyink, G. L. (2005, July). Locality of turbulent cascades. *Physica D: Nonlinear Phenomena*, *207*(1), 91–116. doi: 10.1016/j.physd.2005.05.018

Farrar, J. T., D'Asaro, E., Rodriguez, E., Shcherbina, A., Czech, E., Matthias, P., ... Jenkins, R. (2020, September). S-MODE: The Sub-Mesoscale Ocean Dynamics Experiment. In *IGARSS 2020 - 2020 IEEE International Geoscience and Remote Sensing Symposium* (pp. 3533–3536). doi: 10.1109/IGARSS39084.2020.9323112

Ferrari, R., & Wunsch, C. (2009). Ocean Circulation Kinetic Energy: Reservoirs, Sources, and Sinks. *Annual Review of Fluid Mechanics*, *41*(1), 253–282. doi: 10.1146/annurev.fluid.40.111406.102139

Freilich, M., Flierl, G., & Mahadevan, A. (2022). Diversity of Growth Rates Maximizes Phytoplankton Productivity in an Eddying Ocean. *Geophysical Research Letters*, *49*(3), e2021GL096180. doi: 10.1029/2021GL096180

Germano, M. (1992, May). Turbulence: the filtering approach. *Journal of Fluid Mechanics*, *238*, 325–336. doi: 10.1017/S0022112092001733

Hoskins, B. J., & Bretherton, F. P. (1972). Atmospheric frontogenesis models: Mathematical formulation and solution. *Journal of the Atmospheric Sciences*, *29*(1), 11–37.

Klein, P., & Lapeyre, G. (2009). The Oceanic Vertical Pump Induced by Mesoscale and Submesoscale Turbulence. *Annual Review of Marine Science*, *1*(1), 351–375.

Lapeyre, G., & Klein, P. (2006). Impact of the small-scale elongated filaments on the oceanic vertical pump. *Journal of Marine Research*, *64*(6), 835–851.

Lenain, L., Smeltzer, B. K., Pizzo, N., Freilich, M., Colosi, L., Ellingsen, S., ... Statom, N. (2023). Airborne observations of surface winds, waves and currents from meso to submesoscales. *submitted*.

Lévy, M., Klein, P., & Treguier, A.-M. (2001). Impact of sub-mesoscale physics on production and subduction of phytoplankton in an oligotrophic regime. *Journal of Marine Research*, *59*(4), 535–565.

Mahadevan, A. (2016). The impact of submesoscale physics on primary productivity of plankton. *Annual Review of Marine Science*, *8*, 161–184.

Mahadevan, A., & Tandon, A. (2006). An analysis of mechanisms for submesoscale vertical motion at ocean fronts. *Ocean Modelling*, *14*(3-4), 241–256.

Mauzole, Y. L., Torres, H. S., & Fu, L.-L. (2020). Patterns and Dynamics of SST Fronts in the California Current System. *Journal of Geophysical Research: Oceans*, *125*(2), e2019JC015499. doi: 10.1029/2019JC015499

Mazloff, M. R., Cornuelle, B., Gille, S. T., & Wang, J. (2020). The Importance of Remote Forcing for Regional Modeling of Internal Waves. *Journal of Geophysical Research: Oceans*, *125*(2), e2019JC015623. doi: 10.1029/2019JC015623

McWilliams, J. C. (2016). Submesoscale currents in the ocean. *Proceedings of the Royal Society A: Mathematical, Physical and Engineering Sciences*, *472*(2189), 20160117.

Melville, W. K., Lenain, L., Cayan, D. R., Kahru, M., Kleissl, J. P., Linden, P. F., & Statom, N. M. (2016, June). The Modular Aerial Sensing System. *Journal of Atmospheric and Oceanic Technology*, *33*(6), 1169–1184. doi: 10.1175/JTECH-D-15-0067.1

Naveira Garabato, A. C., Yu, X., Callies, J., Barkan, R., Polzin, K. L., Frajka-Williams, E. E., ... Griffies, S. M. (2022, January). Kinetic Energy Transfers between Mesoscale and Submesoscale Motions in the Open Ocean's Upper Layers. *Journal of Physical Oceanography*, *52*(1), 75–97. doi: 10.1175/JPO-D-21-0099.1

Qiu, B., Chen, S., Klein, P., Sasaki, H., & Sasai, Y. (2014). Seasonal mesoscale and submesoscale eddy variability along the North Pacific Subtropical Countercurrent. *Journal of Physical Oceanography*, *44*(12), 3079–3098.

Rocha, C. B., Chereskin, T. K., Gille, S. T., & Menemenlis, D. (2016). Mesoscale to submesoscale wavenumber spectra in Drake Passage. *Journal of Physical Oceanography*, *46*(2), 601–620.

Rudnick, D. L. (2001). On the skewness of vorticity in the upper ocean. *Geophysical Research Letters*, *28*(10), 2045–2048. doi: 10.1029/2000GL012265

Sandery, P. A., & Sakov, P. (2017, November). Ocean forecasting of mesoscale features can deteriorate by increasing model resolution towards the submesoscale. *Nature Communications*, *8*(1), 1566. doi: 10.1038/s41467-017-01595-0

Schubert, R., Gula, J., Greatbatch, R. J., Baschek, B., & Biastoch, A. (2020, September). The Submesoscale Kinetic Energy Cascade: Mesoscale Absorption of Submesoscale Mixed Layer Eddies and Frontal Downscale Fluxes. *Journal of Physical Oceanography*, *50*(9), 2573–2589. doi: 10.1175/JPO-D-19-0311.1

Shakespeare, C. J. (2016, October). Curved Density Fronts: Cyclogeostrophic Adjustment and Frontogenesis. *Journal of Physical Oceanography*, *46*(10), 3193–3207. doi: 10.1175/JPO-D-16-0137.1

Shcherbina, A. Y., Gregg, M. C., Alford, M. H., & Harcourt, R. R. (2009, November). Characterizing Thermohaline Intrusions in the North Pacific Subtropical Frontal Zone. *Journal of Physical Oceanography*, *39*(11), 2735–2756. doi: 10.1175/2009JPO4190.1

Sinha, A., Callies, J., & Menemenlis, D. (2022, December). Do Submesoscales Affect the Large-Scale Structure of the Upper Ocean? *Journal of Physical Oceanography*, *-1*(aop). doi: 10.1175/JPO-D-22-0129.1

Srinivasan, K., Barkan, R., & McWilliams, J. C. (2023). A Forward Energy Flux at Submesoscales Driven by Frontogenesis. *Journal of Physical Oceanography*, *53*(1), 287–305. doi: 10.1175/JPO-D-22-0001.1

Strobach, E., Klein, P., Molod, A., Fahad, A. A., Trayanov, A., Menemenlis, D., & Torres, H. (2022). Local Air-Sea Interactions at Ocean Mesoscale and Submesoscale in a Western Boundary Current. *Geophysical Research Letters*, *49*(7), e2021GL097003. doi: 10.1029/2021GL097003

Su, Z., Wang, J., Klein, P., Thompson, A. F., & Menemenlis, D. (2018). Ocean submesoscales as a key component of the global heat budget. *Nature communications*, *9*(1), 775.

Thomas, L. N. (2012). On the effects of frontogenetic strain on symmetric instability and inertia–gravity waves. *Journal of Fluid Mechanics*, *711*, 620–640.

# Supporting Information for "Non-linear processes characterize the transition to submesoscale dynamics in observations of a dense filament"

Mara Freilich[1], Luc Lenain[1], Sarah T. Gille[1]

[1]Scripps Institution of Oceanography

## Contents of this file

## 1.   Definitions

The velocity components can be written as the sum of the velocity streamfunction ($\psi$) and velocity potential ($\phi$)

$$u = -\frac{\partial \phi}{\partial x} - \frac{\partial \psi}{\partial y} \tag{1}$$

$$v = -\frac{\partial \phi}{\partial y} + \frac{\partial \psi}{\partial x}. \tag{2}$$

———————

March 20, 2023, 4:36am

The velocity potential is divergent while the streamfunction is rotational.

## 2. Cross spectrum, coherence, and phase

The cross spectrum ($\hat{S}(f)$) is defined as

$$\hat{S}_{uv}(f) = \frac{\langle \hat{u}^* \hat{v} \rangle}{T}, \tag{3}$$

where $\hat{u}$ is the Fourier transform of the $u$ velocity, and $^*$ indicates the complex conjugate (Bendat & Piersol, 2011). The angle brackets indicate averages over $\nu$ realizations. $u$ is the along-track velocity and $v$ is the cross-track velocity. The squared coherence is given by

$$\gamma_{uv}^2(f) = \frac{|\hat{S}_{uv}(f)|^2}{\hat{S}_u(f)\hat{S}_v(f)}. \tag{4}$$

$\hat{S}(f) = \hat{C}(f) + i\hat{Q}(f)$ is complex. The phase is given by

$$\tan(\phi_{uv}(f)) = \left( \frac{-\hat{Q}(f)}{\hat{C}(f)} \right). \tag{5}$$

The 95% percent confidence interval of the kinetic energy spectrum is estimated using a standard method by assuming that the ratio of estimated to true spectrum has a $\chi^2$ distribution with expectation $\nu$ where $\nu$ is the number of segments. The significance of the estimated coherence is assessed using two methods. The 95% significance level is computed as $\sqrt{1 - \alpha^{1/(\nu-1)}}$ where $\alpha = 0.05$. The standard deviation of the coherence is calculated as

$$std_{\gamma_{uv}^2} = \frac{\sqrt{2}(1 - \gamma_{uv}^2)}{|\gamma_{uv}|\sqrt{2\nu}} \tag{6}$$

The standard error of the phase spectrum is calculated as

$$std_{\phi_{uv}} = \frac{\sqrt{1 - \gamma_{uv}^2}}{|\gamma_{uv}|\sqrt{2\nu}} \tag{7}$$

March 20, 2023, 4:36am

## 3. Surface quasigeostrophic model

A surface quasigeostrophic model (SQG) is used to validate the dynamical interpretation of the cross spectrum as representing contributions from ageostrophic advection. The surface quasigeostrophic model describes a flow field where the interior potential vorticity is zero and the full 3D dynamics are described by the 2D surface flow field. This is a suitable null model for this analysis because it is the simplest model that includes surface fronts but not ageostrophic advection. In this model, the interior potential vorticity is zero

$$\nabla^2 \psi + \frac{\partial}{\partial z}\left(\frac{f_0^2}{N_0^2}\frac{\partial \psi}{\partial z}\right) = 0, \tag{8}$$

where $\psi$ is a streamfunction, $f_0$ is the Coriolis frequency, and $N_0$ is the buoyancy frequency. $f_0$ and $N_0$ are both constant. At depth (as $z \to -\infty$), $\psi = 0$. Surface density gradients are advected by and feedback on the streamfunction $\psi$

$$\frac{\partial b}{\partial t} + J(\psi, b) = 0. \tag{9}$$

The surface buoyancy gradients are related to the streamfunction through the hydrostatic relationship $b = \psi_z$. We can solve equation 8 for the streamfunction in Fourier space and obtain

$$\hat{\psi} = \frac{f_0}{N_0}\frac{1}{\kappa}\hat{b} \tag{10}$$

We initialize PyQG (Abernathey et al., 2022), a Python implementation of a surface quasigeostrophic model with two counter-rotating eddies. These eddies evolve to form filaments, but the net kinetic energy flux of the resolved dynamics is always upscale (Capet et al., 2008). A cross spectrum of the $u$ and $v$ velocity components in this model

shows that the cross spectrum is mostly real, particularly at the smallest wavenumbers, in contrast to the observed patterns (Figure S1).

## 4.   Vertical kinetic energy flux terms

While typically only the horizontal terms are considered in spectral kinetic energy fluxes (Aluie et al., 2018; Balwada et al., 2022; Srinivasan et al., 2023), these observations allow us to diagnose kinetic energy fluxes that are associated with the vertical shear. The full expression for the kinetic energy flux is

$$\Pi_a = \underbrace{-(\tau_{uv}(u_y + v_x) + \tau_{uu}u_x + \tau_{vv}v_y)}_{\Pi_h} - \underbrace{(\tau_{uw}u_z + \tau_{vw}v_z)}_{\Pi_v} - \underbrace{(\tau_{ww}w_z}_{\Pi_{ww}} \tag{11}$$

The first term $\Pi_h$ is shown in the main text. The second term, $\Pi_v$, is associated with baroclinicity of the flow. Here we diagnose this term using the velocity and sea surface temperature observations. The third term, $\Pi_w$, cannot be diagnosed with the available observations, but it is expected to be small. We compute $\Pi_v$ by calculating the vertical velocity as $w = \delta \times h$ where $\delta$ is the surface divergence and $h$ is the integration depth. Here, the integration depth is 1 meter, which is the approximate depth over which the surface velocity observations have been averaged (Lenain et al., 2023). The shear terms are computed from thermal wind balance. However, given that only sea surface temperature observations are available, we convert sea surface temperature to density using thermosalinograph observations from a ship that was nearby. The observed fronts are partially salinity compensated so the density is computed from temperature using a relationship within the observed temperature range. We find that $\Pi_v$ peaks at the front, where $\delta$ is large, and is negative while $\Pi_h$ is positive (Figure S4) However, $\Pi_v$ is still at least an order of magnitude smaller than $\Pi_h$.

<center>March 20, 2023, 4:36am</center>

## References

Abernathey, R., rochanotes, Ross, A., Jansen, M., Li, Z., Poulin, F. J., ... Tobias (2022, May). *pyqg/pyqg: v0.7.2.* Zenodo. Retrieved 2023-03-17, from `https://zenodo.org/record/6563667`  doi: 10.5281/zenodo.6563667

Aluie, H., Hecht, M., & Vallis, G. K. (2018, February). Mapping the Energy Cascade in the North Atlantic Ocean: The Coarse-Graining Approach. *Journal of Physical Oceanography*, *48*(2), 225–244. Retrieved 2022-08-23, from `https://journals.ametsoc.org/view/journals/phoc/48/2/jpo-d-17-0100.1.xml` (Publisher: American Meteorological Society Section: Journal of Physical Oceanography) doi: 10.1175/JPO-D-17-0100.1

Balwada, D., Xie, J.-H., Marino, R., & Feraco, F. (2022, October). Direct observational evidence of an oceanic dual kinetic energy cascade and its seasonality. *Science Advances*, *8*(41), eabq2566. Retrieved 2023-03-20, from `https://www.science.org/doi/full/10.1126/sciadv.abq2566` (Publisher: American Association for the Advancement of Science) doi: 10.1126/sciadv.abq2566

Bendat, J. S., & Piersol, A. G. (2011). *Random Data: Analysis and Measurement Procedures.* John Wiley & Sons.

Capet, X., Klein, P., Hua, B. L., Lapeyre, G., & Mcwilliams, J. C. (2008, June). Surface kinetic energy transfer in surface quasi-geostrophic flows. *Journal of Fluid Mechanics*, *604*, 165–174. Retrieved 2023-03-17, from `https://www.cambridge.org/core/journals/journal-of-fluid-mechanics/article/surface-kinetic-energy-transfer-in-surface-quasigeostrophic-flows/`

5AEDA38EF14C0C33AA1AC073BCF51087  (Publisher: Cambridge University Press) doi: 10.1017/S0022112008001110

Lenain, L., Smeltzer, B. K., Pizzo, N., Freilich, M., Colosi, L., Ellingsen, S., ... Statom, N. (2023). Airborne observations of surface winds, waves and currents from meso to submesoscales. *submitted*.

Srinivasan, K., Barkan, R., & McWilliams, J. C. (2023). A Forward Energy Flux at Sub-mesoscales Driven by Frontogenesis. *Journal of Physical Oceanography*, *53*(1), 287–305. Retrieved 2023-03-20, from https://journals.ametsoc.org/view/journals/phoc/53/1/JPO-D-22-0001.1.xml  (Publisher: American Meteorological Society Section: Journal of Physical Oceanography) doi: 10.1175/JPO-D-22-0001.1
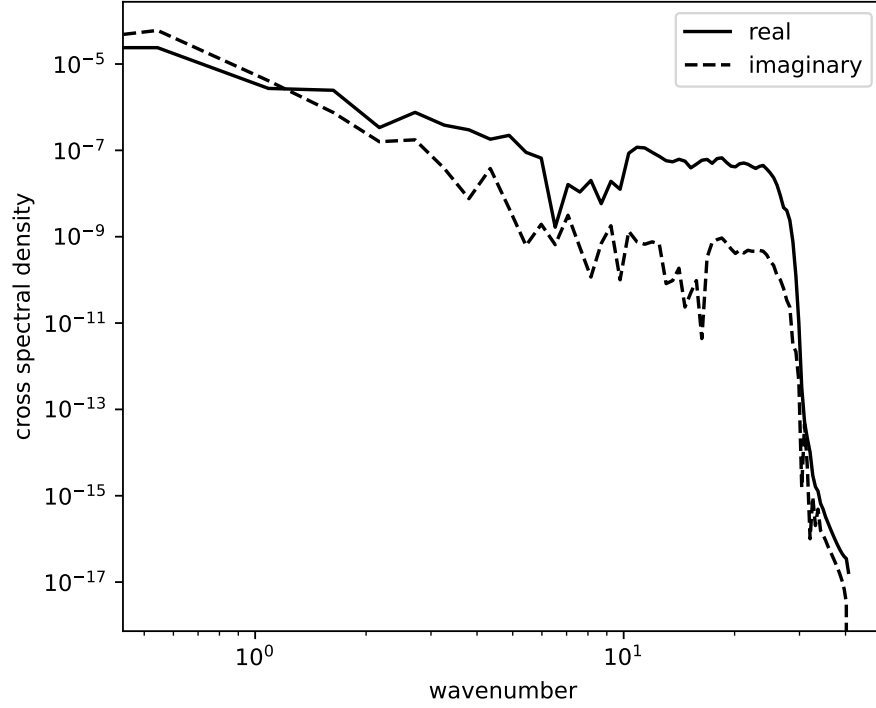
**Figure S1.** Cross spectrum as a function of wavenumber from a surface quasigeostrophic model initialized with two counter rotating eddies. The SQG model used is PyQG. The model is non-dimensionalized with buoyancy frequency and Coriolis frequency equal, as is approximately the case in the surface layer here. The solid line is the real part of the cross spectrum while the dashed line is the imaginary part. In contrast to the observations where the imaginary part becomes relatively more important at small scales, in the SQG model the imaginary part becomes less important at small scales.
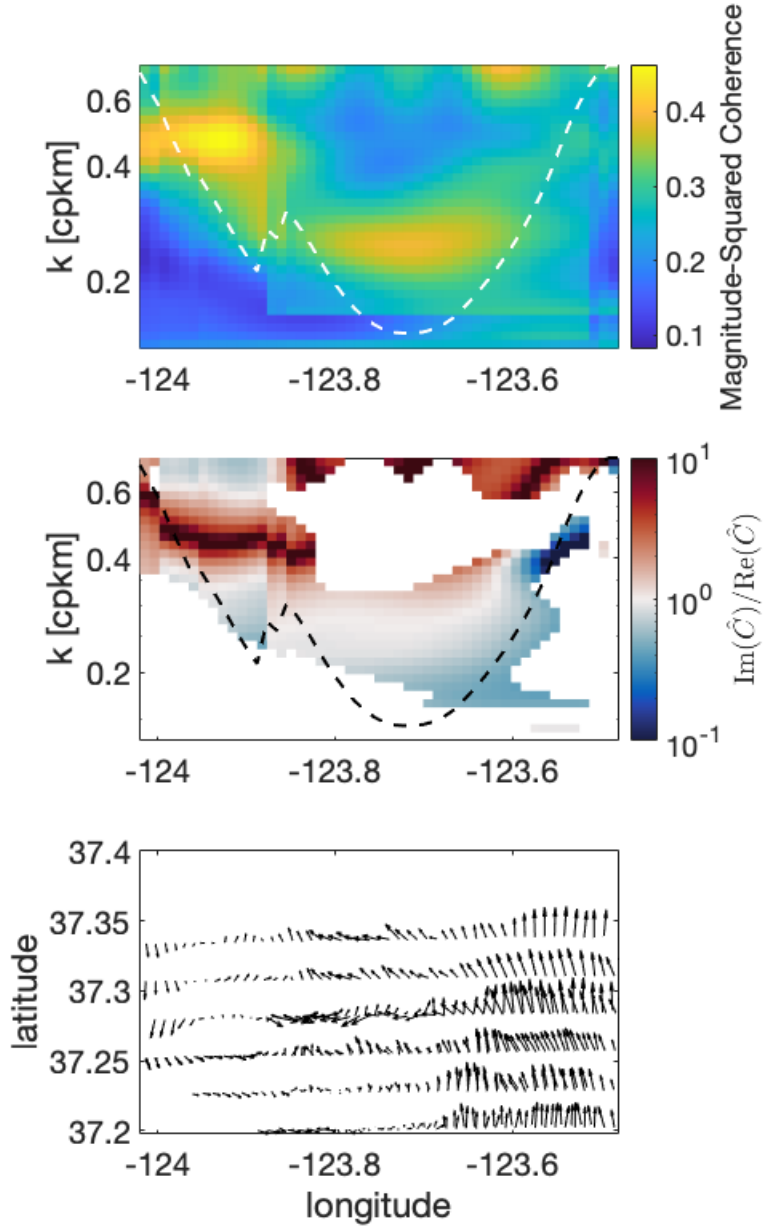
**Figure S2.** (top) Average wavelet coherence spectrum from S-MODE (middle) Ratio of the imaginary to real part of the cross spectrum. This ratio is only shown where the coherence value is above the significance threshold. (bottom) Velocity vectors. This analysis reveals that the shift from a predominantly real to a complex cross spectrum occurs at the strongest fronts in the region sampled, occurring at slightly larger scales at the western front and slightly smaller scales at the eastern fronts.
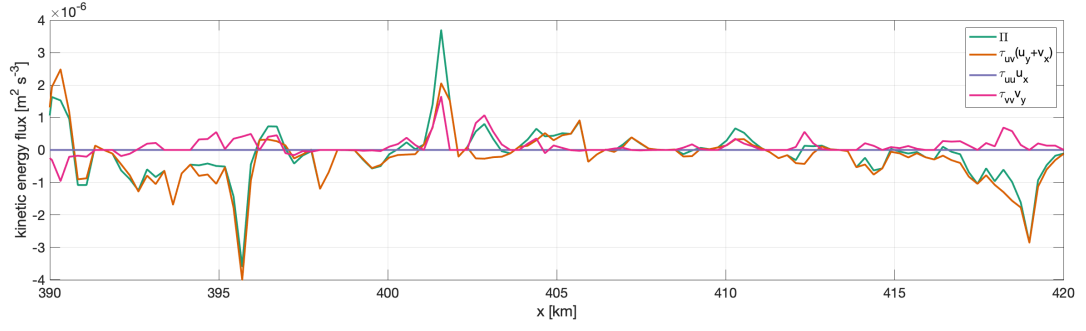
**Figure S3.** Kinetic energy flux across 1 km ($\Pi$) and its component parts $\Pi = -(\tau_{uv}(u_y + v_x) + \tau_{uu}u_x + \tau_{vv}v_y)$.
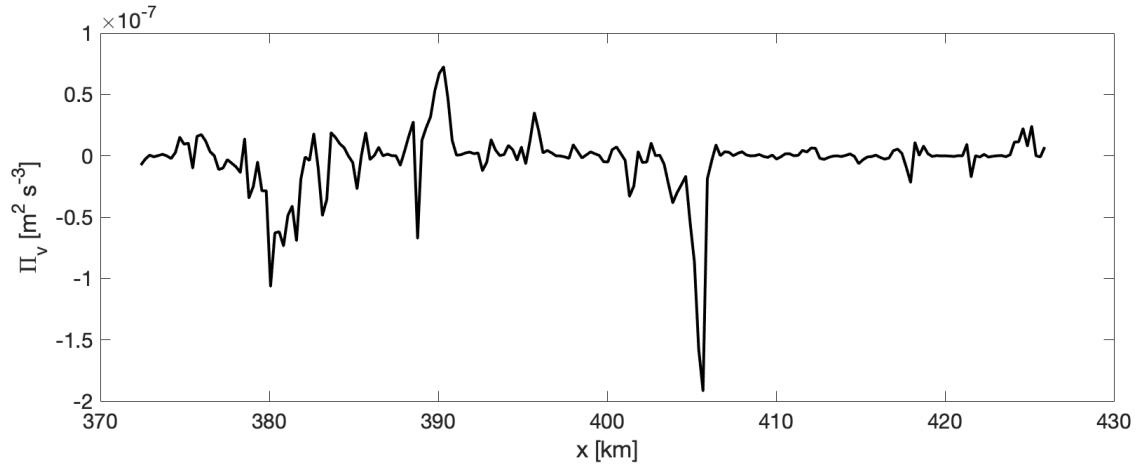


**Figure S4.** Kinetic energy flux associated with vertical shear $\Pi_v$ across 1 km.

March 20, 2023, 4:36am